Supporting Information

In Situ Photo-Fenton-like Reaction and Oxygen Evolution through Polaron-Mediated WO_3

Ardiansyah Taufik[1,*], *Akira Yoko*[1,2,*], *Chunli Han*[1], *Wahyudiono*[3], *Satoshi Ohara*[4], *Tadafumi Adschiri*[1,4,*]

[1]WPI – Advanced Institute for Materials Research (WPI-AIMR), Tohoku University, 2-1-1 Katahira, Aoba-ku, Sendai, Miyagi 980-8577, Japan

[2]International Center for Synchrotron Radiation Innovation Smart (SRIS), Tohoku University, Aramaki Aza-Aoba, Aoba-ku, Sendai, 980-8572, Japan

[3]Department of Chemical Engineering, Institut Teknologi Sepuluh Nopember, Kampus ITS Sukolilo, Surabaya, 60111, Indonesia

[4]New Industry Creation Hatchery Center, Tohoku University, Sendai 980-8579, Japan

S1. Table S1. HCl concentration and sample name list.

HCl Volume (mL)	Moles HCl = Volume × 0.0121	Total Volume (mL) = 200 + HCl	Total Volume (L)	[H^+] (mol/L)	Sample name
15 mL	15 × 0.0121 ≈ **0.1815 mol**	215	0.215 L	**0.844 mol/L**	[H^+] = 0.8
30 mL	30 × 0.0121 ≈ **0.363 mol**	230	0.230 L	**1.578 mol/L**	[H^+] = 1.6
60 mL	60 × 0.0121 ≈ **0.726 mol**	260	0.260 L	**2.792 mol/L**	[H^+] = 2.8
180 mL	180 × 0.0121 ≈ **2.178 mol**	380	0.380 L	**5.732 mol/L**	[H^+] = 5.7

S2. Catalytic reaction set-up

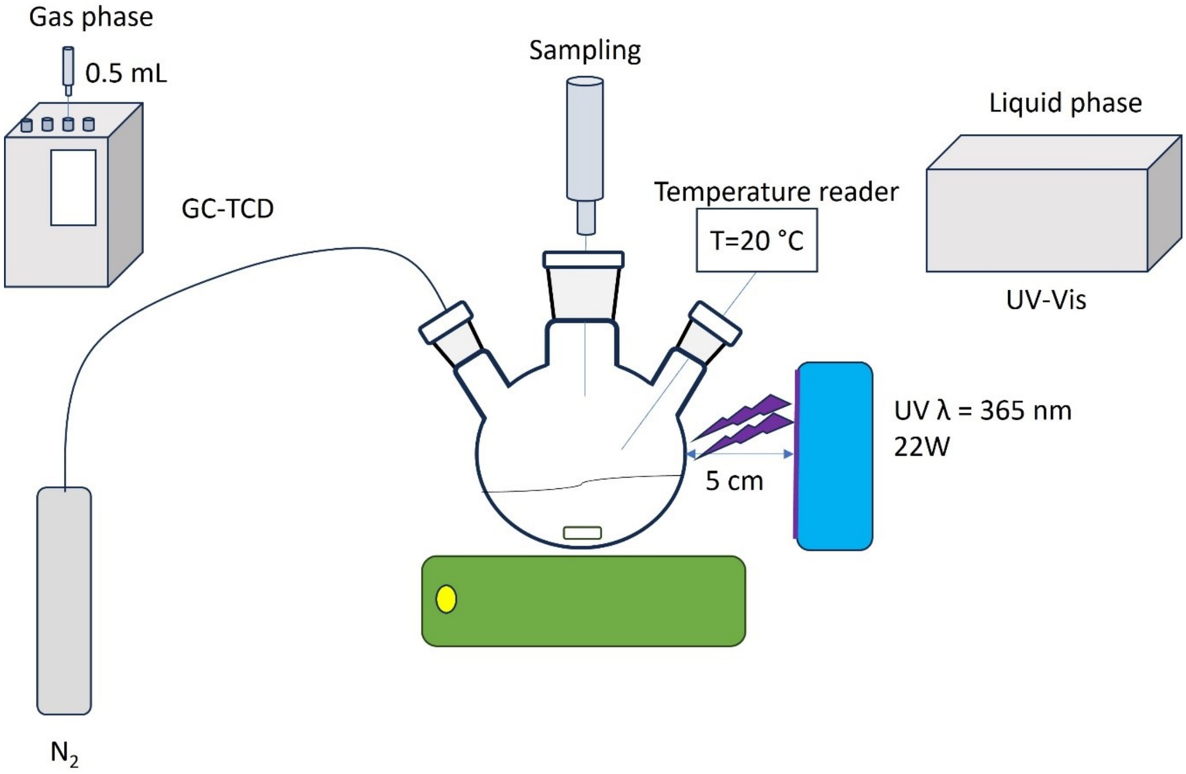

Figure S1. Catalytic reaction system.

Power density calculation

$$E = \frac{P}{4\pi r^2}$$

$r = distance\ lamp\ to\ the\ reactor\ (cm)$

$P = UV\ lamp\ power\ (Watt)$

$$E = \frac{22\ Watt}{4\pi(5)^2}$$

$E \approx 70\ mW\ cm^2$

- **Calibration of O_2 gas**

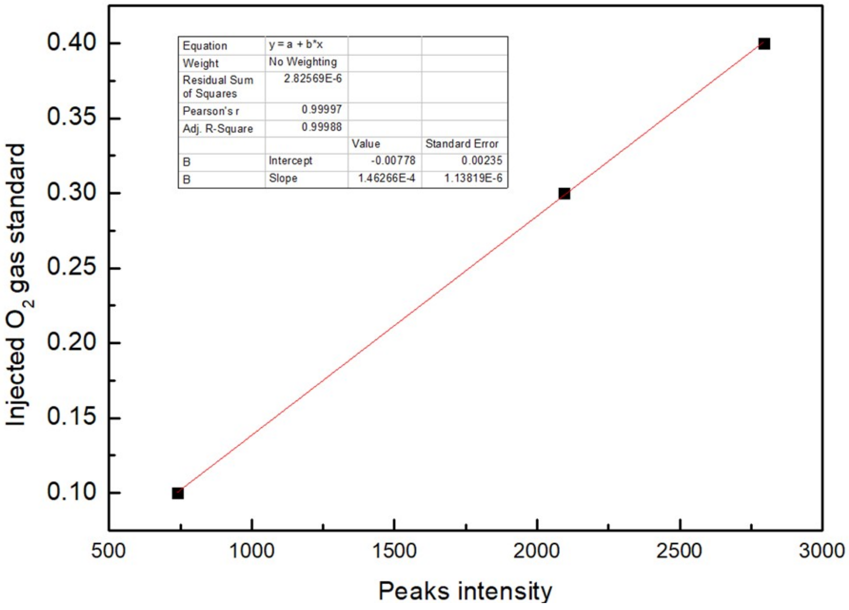

Equation	y = a + b*x		
Weight	No Weighting		
Residual Sum of Squares	2.82569E-6		
Pearson's r	0.99997		
Adj. R-Square	0.99988		
		Value	Standard Error
B	Intercept	-0.00778	0.00235
B	Slope	1.46266E-4	1.13819E-6

Figure S2. Calibration data for O_2 gas.

S3. Gas detection results during Photo-Fenton reaction

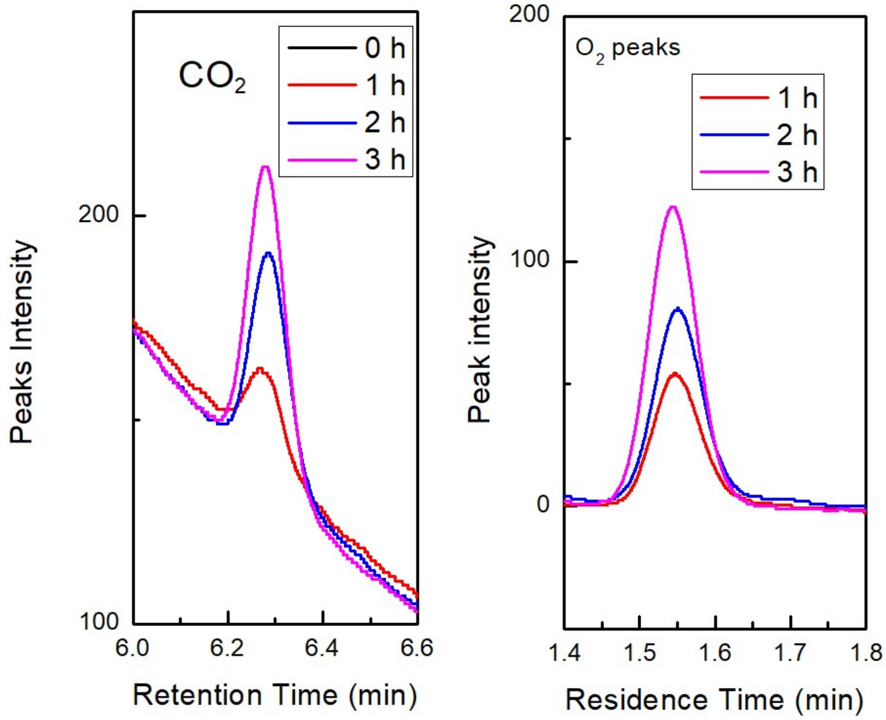

Figure S3. CO_2 gas and O_2 gas produced during photo-Fenton like reaction.

S4. O_2 evolution rates data for H_2O_2 + UV, WO_3+ UV, and WO_3 + H_2O_2 + UV

Table S2. Data O_2 evolution rates of H_2O_2 + UV, WO_3+ UV, and WO_3 + H_2O_2 + UV

Sample	O_2 evolution rates (mmol g^{-1} h^{-1})
H_2O_2 + UV	0.21
WO_3 + UV	0.80
WO_3 + H_2O_2 + UV	1.62

S5. Analysis of supersaturation control on the nucleation of H_4WO_5

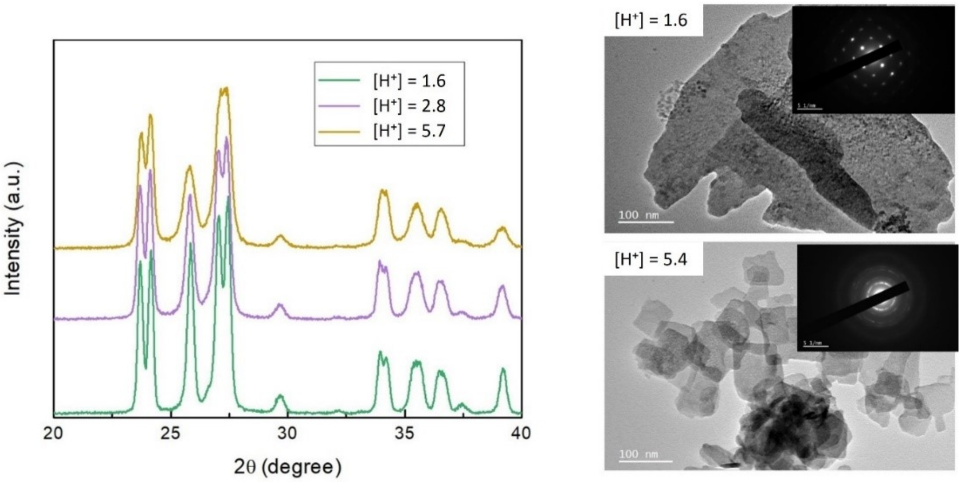

Figure S4. XRD of H_4WO_5 with different proton concentration and TEM images at protonation of $[H^+] = 1.6$ and $[H^+] = 5.7$.

S6. Analysis of Acid Orange 7 Adsorption at different protonation samples

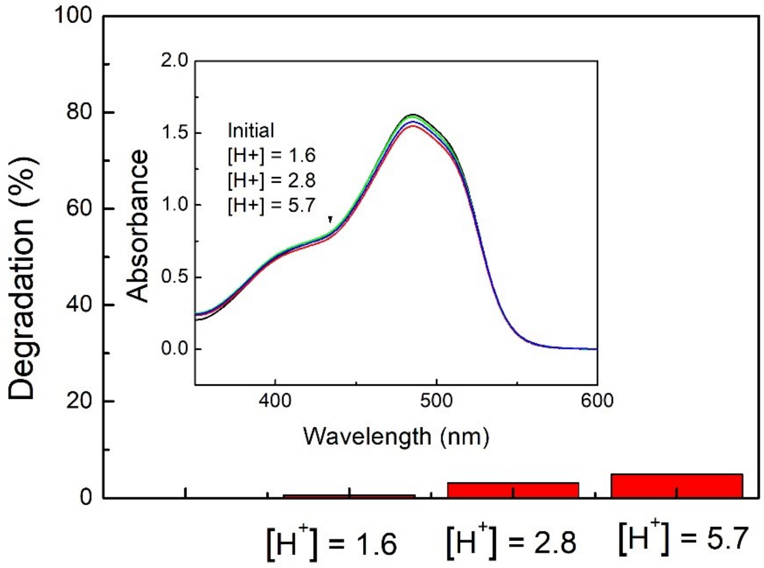

Figure S5. Acid Orange 7 adsorption ability of WO_3 at different protonation samples.

S7. Surface charge analysis

The zeta potential analysis in **Figure S6** (a) shows that the surface charge of WO_3 follows a consistent trend: at high pH, the particles exhibit a negative surface charge; at low pH, the charge becomes neutral; and at very low pH, the surface becomes positively charged. These surface charge characteristics are directly correlated with the photo-Fenton reaction behavior. For anionic pollutants such as Acid Orange 7, stronger adsorption and interaction occur at low pH, where the positively charged WO_3 surface enhances electrostatic attraction. In contrast, for cationic pollutants such as methylene blue, the opposite trend is expected. The photo-Fenton results for $[H^+] = 5.7$ at different pH values clearly demonstrate this phenomenon, as presented in **Figure S6(b) and (c).**

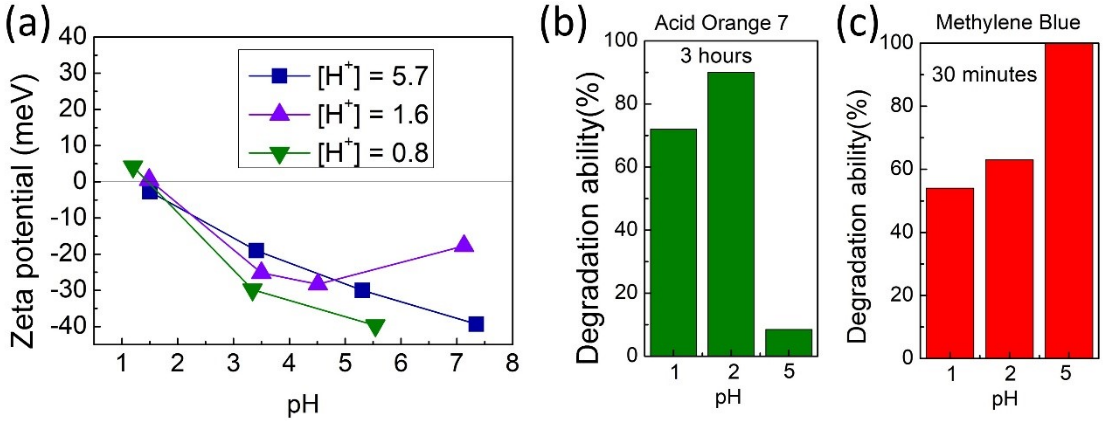

Figure S6. (a) Zeta potential analysis of WO_3 at different protonation levels. Photo-Fenton like reactions at different pH for (b) Acid Orange 7 and (c) Methylene Blue for $[H^+] = 5.7$ sample.

S8. Analysis photo-Fenton reactions with defect and without defect analysis.

The XRD patterns in **Figure S7(a)** show that the WO_3 $[H^+] = 5.7$ samples exhibit no significant structural differences when annealed under different atmospheres. However, the defect-site analysis obtained from the EPR spectra in **Figure S7(b)** reveals that the sample annealed under an N_2 atmosphere displays a clear splitting signal, indicating a higher concentration of W^{5+} species. However, the surface area plotted in **Table S3** has demonstrated that the value does not significantly change. The photo-Fenton-like reaction results (**Figure S7(c)-(d))** further confirm that samples with higher internal W^{5+} defect concentrations exhibit superior degradation performance toward Acid Orange 7, highlighting the crucial role of W^{5+} in the photo-Fenton-like degradation process.

Furthermore, the analysis was extended by evaluating the ratios of degradation rate to W^{5+} concentration and degradation rate to surface area at different protonation levels (**Figure (S8 (a)-(c)**)). Both sets of data show an increasing trend, indicating that surface area and W^{5+} defects act synergistically to enhance the photo-Fenton-like reaction kinetics.

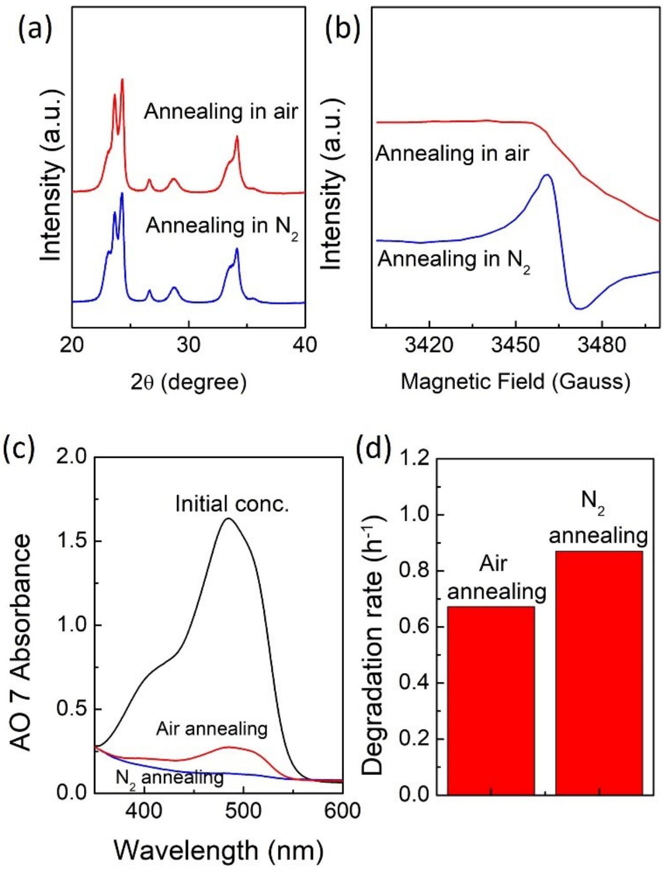

Figure S7. (a) XRD and (b) EPR spectra of WO^3 $[H^+] = 5.7$ spectra at different annealing atmospheres. (c) absorption spectra of Acid Orange 7 after photo-Fenton reaction with different treatment samples. (d) rate constant of Acid Orange 7 degradation with different annealing treatment samples.

Table S3. Surface area of WO^3 $[H^+] = 5.7$ at different annealing treatment.

Sample	Surface area (m^2 g^{-1})
$[H^+] = 5.7$ annealing in air	37
$[H^+] = 5.7$ annealing in N_2	30

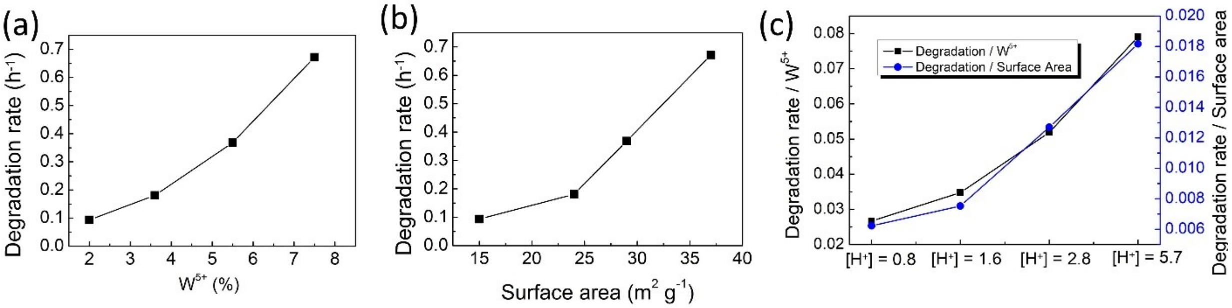

Figure S8. (a) Degradation rate vs W^{5+} (%), (b) Degradation rate vs Surface area. (c) Degradation rate per W^{5+} and degradation per surface area of Acid orange 7 degradation at different protonation samples.

S9. Impurity analysis

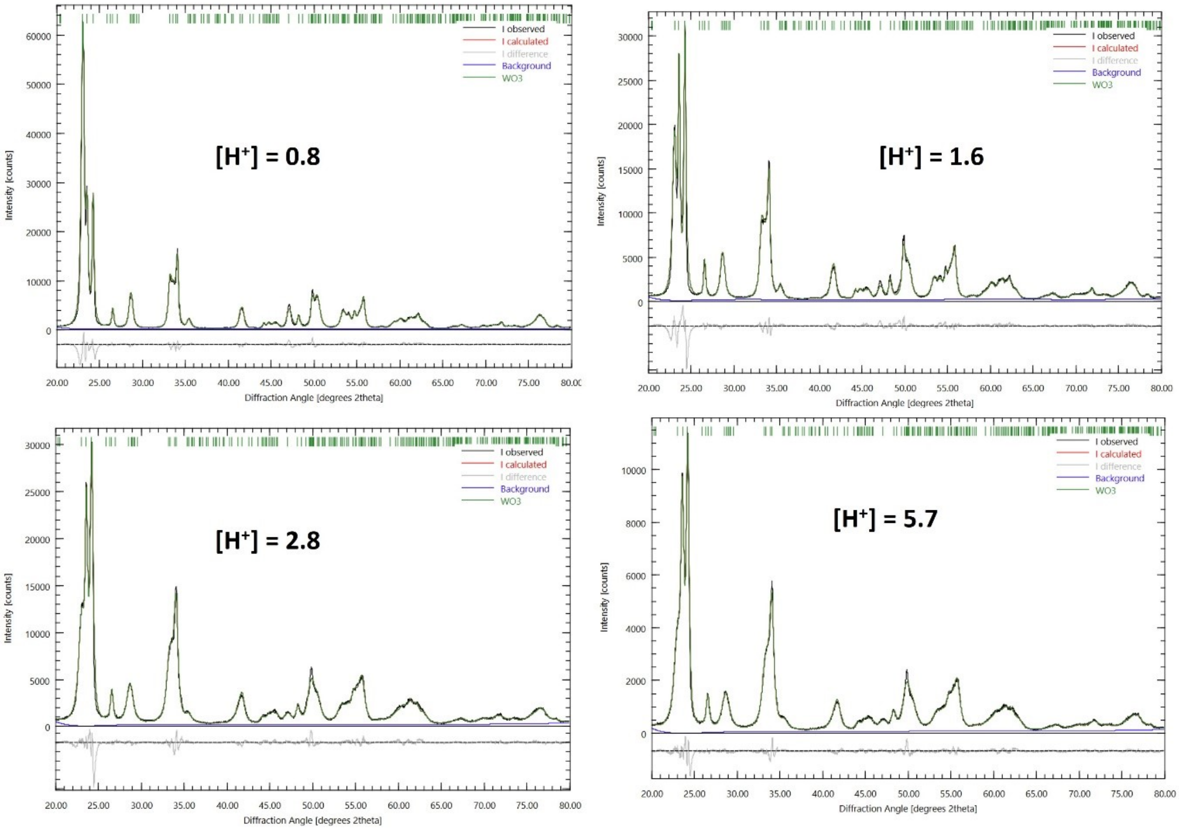

Figure S9. XRD Rietveld refinement results for all samples.

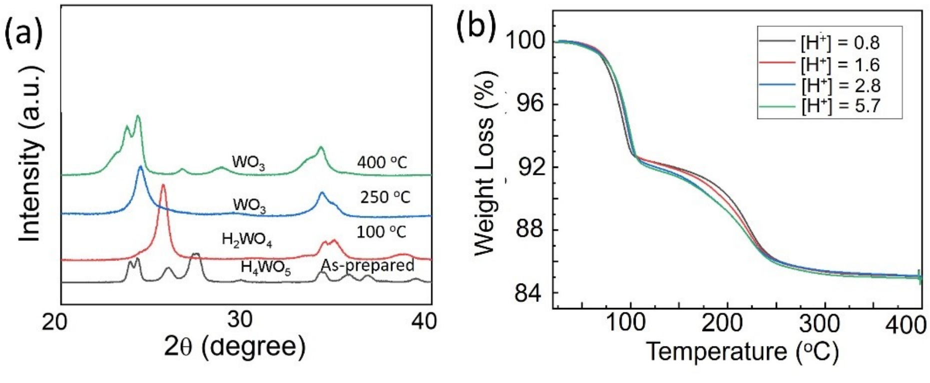

Figure S10. (a) XRD spectra of WO_3 precursor at different annealing temperatures. (b) TGA analysis of WO_3 at different protonation level.

The XRD analysis confirms that all WO_3 samples were successfully synthesized without any detectable impurities. This conclusion is supported by **Figure S10(a)**, which shows that H_4WO_5 is fully transformed into WO_3 at 250 °C. The TGA results (**Figure S10(b)**) further corroborate this finding, indicating that no additional phase transitions occur during annealing up to 400 °C.

S10. Lattice analysis

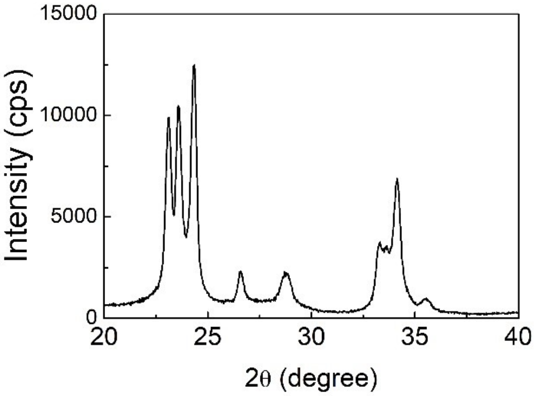

Figure S11. XRD spectra of high crystalline WO_3 obtained from continuous low reactor hydrothermal synthesis at supercritical conditions.

Table S4. Lattice parameters analysis of WO_3 at different protonation.

Sample [H^+]	Lattice parameters (Å)			Lattice Volume (Å^3)	Lattice Volume Strain (%)
	a	b	c		
High crystalline WO_3	7.312	7.5328	7.695	423.83	
0.8	7.321	7.528	7.707	424.75	0.21
1.6	7.329	7.525	7.707	425.04	0.28
2.8	7.332	7.53	7.715	425.94	0.49
5.7	7.342	7.54	7.717	427.20	0.79

S11. Photoluminescence and XPS W4f spectra for [H$^+$] = 1.6 and [H$^+$] = 5.7 samples.

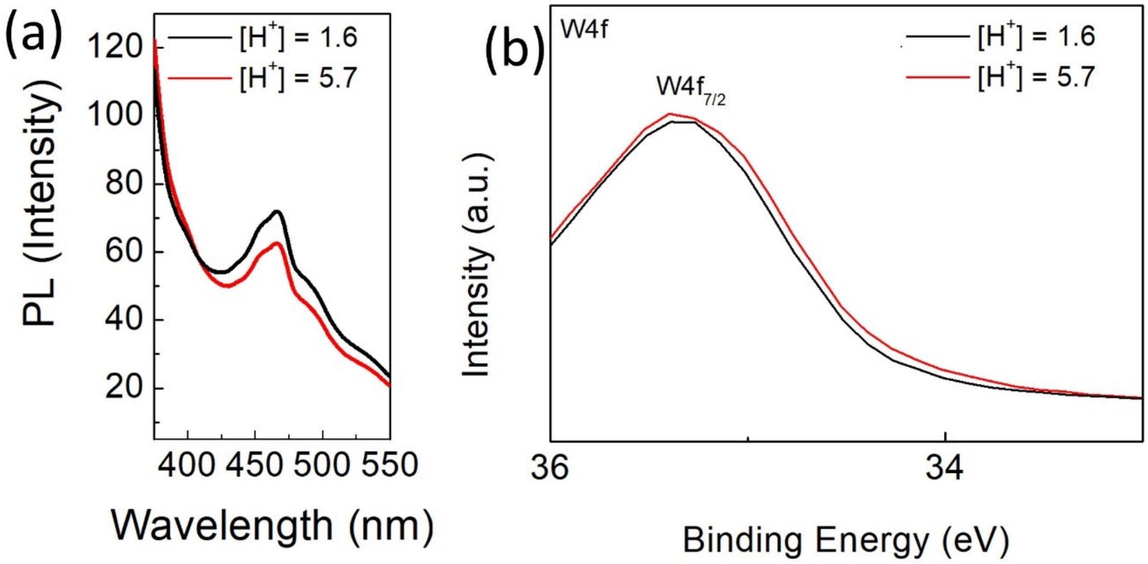

Figure S12. (a) Photoluminescence spectra and (b) XPS spectra of W 4f states for [H$^+$] = 1.6 and [H$^+$] = 5.7 samples.

S12. Density functional theory (DFT) calculation:

DFT calculation was performed by Winmostar software (Winmostar V10, X-Ability Co. Ltd., Tokyo, Japan, 2020) with the quantum espresso calculation package.[2] The 2 x 2 x 1 supercell of monoclinic WO_3 with 64 atoms were used. Their Brillouin zone samplings were carried out by using 2 × 2 × 1 *k*-points. For the exchange-correlation energy, the Perdew-Burke-Brinkerhoff (PBE)[3] functional was used while the adsorption correlation energies are described by the projector-augmented wave (PAW)[4]. The convergence criteria during the geometry optimization were adjusted as follows: The total energy and the forces are 10^{-5} eV and 0.1 eV/Å, respectively. The strain structure was given by manually changing the lattice parameters as desired and conduct ionic relaxation on the structure.

The formation energy was calculated by the following equation: The surface energy and the adsorption energy and charge differences were calculated by using the following equations:

$$E_{form} = E_{defect} - E_{perfect} + \mu_o$$

Where: E_{defect} is the total energy of WO_3 with one oxygen atom removed and $E_{perfect}$ is the total energy of pristine WO_3 and μ_o is the chemical potential of oxygen (typically $\leq \frac{1}{2}E(O_2)$). The calculated formation energy is around 4.3 eV and 4.4 eV.

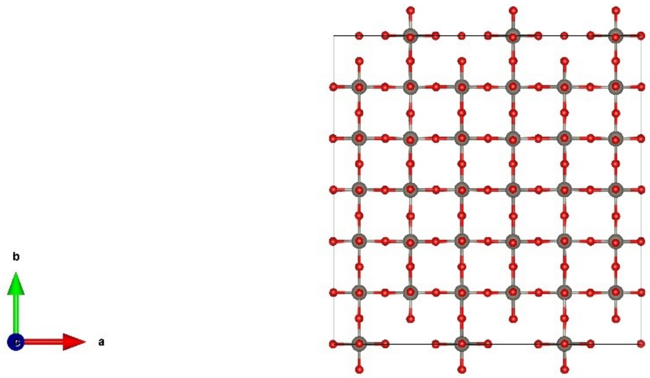

Figure S13. Model WO_3 structure.

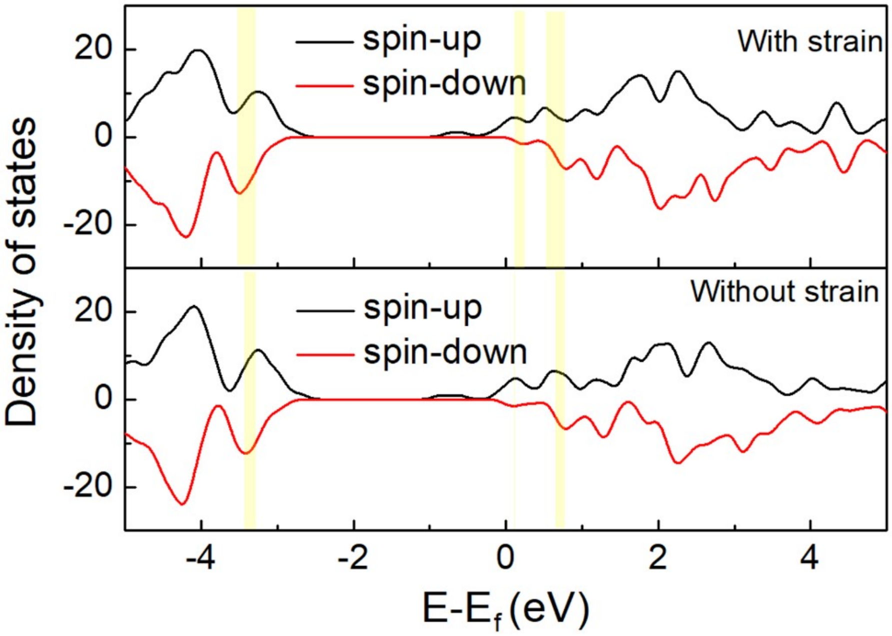

Figure S14. Spin-polarized density of states after addition of one electron for with and without strain model.

Table S5. Total magnetization results with and without strain model.

Model	**Spin-polarized total magnetization**
Without strain	2.83 μB
With strain	3.14 μB

For confirming the improvement of electron localization after strain, spin polarized calculation density functional calculation was conducted for strained and non-strained structure upon the addition of an extra electron. The results revealed that the total magnetization rises from 2.83 μB in the unstrained structure to 3.14 μB (**Table S3**) in the strained structure indicating enhanced local spin polarization. This argument is also supported by density of states measurement which shows the higher asymmetrical behavior between spin-up and spin-down (**Figure S14**). This increase in magnetization reflects the stabilization of localized unpaired electrons. When strain exist, it alters the crystal symmetry and strengthens electron–phonon coupling, creating favorable conditions for localized electrons. These findings suggest that lattice strain facilitates the generation of W^{5+} species by creating a more favorable environment for electron trapping, thereby contributing to the improved photocatalytic activity of WO_3 in photo-Fenton reactions.